2024 NATIONAL CONFERENCE ON HIGH VOLTAGE AND DISCHARGE PLASMAS

Numerical investigation of plasma CO_2 hydrogenation in a coaxial dual-layer dielectric barrier discharge at atmospheric pressure

To cite this article: Jing LI *et al* 2025 *Plasma Sci. Technol.* **27** 084005

Plasma Sci. Technol. **27** (2025) 084005 (15pp)
https://cstr.cn/32219.14.2058-6272/ade8db
https://doi.org/10.1088/2058-6272/ade8db

Numerical investigation of plasma CO_2 hydrogenation in a coaxial dual-layer dielectric barrier discharge at atmospheric pressure

Jing LI (李晶)[1], **Chunjing WANG** (汪纯婧)[1], **Hancheng XU** (徐汉城)[1], **Kaiyue GAO** (高凯悦)[1], **Bingyan DONG** (董冰岩)[2], **Chuanjie CHEN** (陈传杰)[3], **Tongbiao WANG** (王同标)[1], **Muyang QIAN** (钱沐杨)[1,*], **Jialiang ZHANG** (张家良)[4] **and Dezhen WANG** (王德真)[4]

[1] School of Physics and Materials Science, Nanchang University, Nanchang 330031, People's Republic of China
[2] School of Emergency Management and Safety Engineering, Jiangxi University of Science and Technology, Ganzhou 341000, People's Republic of China
[3] School of Information Engineering, Yancheng Institute of Technology, Yancheng 224051, People's Republic of China
[4] School of Physics, Dalian University of Technology, Dalian 116024, People's Republic of China

[*]E-mail of corresponding author: qianmuyang@ncu.edu.cn

Received 28 April 2025, revised 25 June 2025
Accepted for publication 26 June 2025
Published 18 July 2025

Abstract

Atmospheric-pressure non-equilibrium plasma is emerging as a promising technology for catalyzing CO_2 hydrogenation into valuable oxygenated chemicals at ambient temperatures, making it a focal point under current dual-carbon policies. This paper presents a 2D fluid model for plasma CO_2 hydrogenation using coaxial dual-layer dielectric barrier discharge at atmospheric pressure. This research investigates streamer discharge characteristics induced by varying feed gas volume ratios, positive and negative nanosecond pulsed excitations, and the presence or absence of dielectric sphere filling. The results indicate that increasing hydrogen content in the feed gas under positive nanosecond pulses enhances electron density, local electric field strength, and electron temperature at the streamer forefront, the streamer propulsion speed is faster, and the streamer morphology becomes more convergent. Moreover, higher hydrogen content facilitates methanol synthesis. When the excitation voltage is a negative nanosecond square wave pulse, the higher electron density, spatial electric field and electron temperature are primarily concentrated on the inner dielectric surface, and the streamer is more dispersed, filling the entire gap, exhibiting discharge characteristics distinctly different from those of the positive pulse streamer.

Keywords: coaxial dual-layer dielectric barrier discharge, CO_2 hydrogenation, positive and negative streamers, reaction mechanism

(Some figures may appear in colour only in the online journal)

* Author to whom any correspondence should be addressed.

1. Introduction

CO_2, a greenhouse gas, has significantly increased at atmospheric levels due to human activities, thereby exacerbating the greenhouse effect. By 2023, global CO_2 emissions from fossil fuels had resumed an upward trajectory, reaching record levels of 36.8 billion tones—a 1.1% increase from 2022 [1]. Strategies to mitigate CO_2 excess include carbon capture and storage, carbon capture and utilization, and carbon capture and recovery, highlighting the urgency of converting CO_2 into valuable chemicals and fuels as a critical challenge of the 21st century [2]. A prevalent approach involves co-oxidizing CO_2 with hydrogen-source reactants such as CH_4, H_2 and H_2O to produce valuable oxygenated compounds such as methanol, formaldehyde, dimethyl ether and formic acid. Methanol is particularly esteemed for its clean energy attributes, ease of storage and transport, making CO_2-to-methanol synthesis a feasible solution.

Given the robust stability due to strong carbon-oxygen bonds (283 kJ/mol) and a Gibbs free energy of −394 kJ/mol, CO_2 conversion benefits when paired with reactants of higher Gibbs free energy (less negative). Hydrogen (Gibbs free energy ΔG = 0 kJ/mol), for example, contributes its inherent chemical energy to effectively drive CO_2 conversion [3]. Splitting CO_2 molecules necessitates substantial energy and typically occurs under catalytic reaction conditions with elevated temperatures and pressures, which can result in significant environmental pollution and adverse impacts [4]. The considerable mass disparity between electrons and heavy plasma particles ensures minimal energy loss in elastic collisions, facilitating rapid energy absorption from electric fields. These electrons act as catalysts within non-thermal plasmas at atmospheric pressure, generating highly reactive chemical combinations and energized electrons capable of dissociating CO_2 molecules at ambient temperatures [3]. Thus, plasma technology offers a promising approach for CO_2 conversion, supported by extensive research in this field [5, 6]. Various types of plasma devices utilized for CO_2 conversion include dielectric barrier discharge (DBD) [7–9], gliding arc discharge (GA) [10–12], glow discharge [13–15], corona discharge [16–18] and microwave discharge (MW) [19, 20]. Among them, atmospheric DBD is a promising reactor due to its strong plasma chemical activity, low gas temperature, and ability to easily incorporate various catalytic particles. In addition, it can effectively balance energy efficiency, conversion rate and economic benefits.

Previous researchers have conducted significant research into atmospheric-pressure non-equilibrium plasma CO_2 splitting and catalytic conversion, emphasizing a combined approach of experimental diagnostics and numerical simulations. Experimental diagnostics encompasses electrical and optical techniques, such as voltage and current waveforms measurement, Lissajous graphical power calculations, emission spectroscopy (OES), ICCD high-speed imaging, and chemical analysis via gas chromatography/mass spectrometry. Numerical simulations utilize fluid models, hybrid models, etc, as a tool to support experimental diagnostics for mechanistic studies. Douat *et al* experimentally investigated the dissociation of CO_2 in symmetric point-to-point DBDs [21]. The results indicated that the CO_2 conversion rate is primarily dependent on the specific energy input rather than the geometric configuration of the DBD. Barkhordari *et al* designed a DC shunt operation for an atmospheric-pressure Ar/CO_2 mixed gas plasma jet [22]. They demonstrated that increasing the input current results in higher electron number density and improved efficiency in decomposing CO_2 into CO, O_2 and O. Wang *et al* designed four coaxial cylindrical dielectric barrier discharge micro-plasma reactors, aimed at the non-catalytic decomposition of pure CO_2 into CO and O_2 under conditions of low temperature and atmospheric pressure [23]. The study concluded that incorporating segmented outer electrodes enhances CO_2 decomposition, leading to higher CO_2 conversion rates and energy efficiencies in segmented outer-electrode micro-plasma reactors. Navascués *et al* attempted to enhance conversion and energy efficiency in a parallel plate packed-bed plasma reactor by utilizing lead titanate as the ferroelectric material, aiming to avoid generating harmful N_XO_Y by-products [24]. CO_2 hydrogenation for the synthesis of high-value oxygen-containing compounds has also been a hot topic in recent years [25, 26]. Wang *et al* suggested that employing bimetallic Ni-Co catalysts in synergistic plasma-catalyzed CO_2 hydrogenation to methanol significantly enhances methanol selectivity and CO_2 conversion [25]. Zhang *et al* designed a dielectric barrier discharge reactor to study the electron-induced and thermochemical effects on CO_2 hydrogenation [27]. The findings indicated that CO_2 conversion depended on discharge mode and electron density, rather than electron energy. Zeng *et al* explored plasma-catalyzed CO_2 hydrogenation using various catalysts at different temperatures [28]. The study revealed that plasma catalysis greatly enhances CO_2 conversion, with SiO_2 demonstrating stronger catalytic activity compared to an Al_2O_3-supported catalyst. Cui *et al* conducted experimental research on plasma co-catalyst catalyzed CO_2 hydrogenation to methanol, demonstrating that this approach can enhance CO_2 conversion by 10% and increase CH_3OH selectivity to 65% [29]. Sun *et al* investigated the CO_2 hydrogenation process using Pd/ZnO and ZnO in a tubular DBD reactor under atmospheric pressure [30]. The study revealed that DBD combined with Pd/ZnO catalysts nearly doubled both CO_2 conversion (36.7%) and CO_2 yield (35.5%). Fuente *et al* explored surface wave plasma hydrogenation of CO_2 in order to produce high-value chemicals [26]. They examined how gas volume ratio, gas flow rate and specific energy input affect reaction performance. Experimental findings indicated that increasing the initial hydrogen content in the reaction gas raised electronic excitation temperature and electron density. Wang *et al* achieved atmospheric-pressure room-temperature DBD synergistic catalyst CO_2 hydrogenation to synthesize high-value methanol [31]. They primarily investigated the effects of different electrode structures in reactors, catalytic synergy,

and gas volume ratios on methanol synthesis. The results indicated that the unique water-grounded electrode exhibited optimal reaction performance. With increasing initial hydrogen content in the reaction gas, the methanol content in the products also increased.

In atmospheric-pressure non-equilibrium plasmas, the short electron mean free path and the high electron collision frequency led to inadequate experimental diagnostic methods to accurately determine the core discharge parameters, especially for the carbon dioxide or carbon dioxide-rich plasma discharges. The main reasons are as follows. First, the atmospheric DBD in carbon dioxide or carbon dioxide-rich mixture is not spatially homogeneous but consists of numerous filamentary microdischarges (FMs) that occur randomly in both time and space along the axial and radial directions, making experimental optical diagnostics difficult to conduct. Second, there is no efficient photoionization in carbon dioxide or carbon dioxide-rich gas plasma since photons in the relevant energy range are rapidly absorbed, causing there to be two to three orders of magnitude lower than that in air. Specifically, the photon absorption length in carbon dioxide is only 6.1–40 μm at standard temperature and pressure, while in air it is much longer, ranging from 33 μm to 1.9 mm [32, 33]. Thus, the streamers propagate more stochastically, and they could eventually branch further presenting challenges for experimental diagnostics. Finally, when catalyst beads are filled in the DBD reaction chamber (Packed-Bed Dielectric Barrier Discharge, PBDBD), experimental optical diagnostics becomes more difficult to perform. Therefore, it is highly necessary to develop specific plasma discharge models related to CO_2 dissociation and hydrogenation, as well as conduct numerical simulations to advance research in this critical area. Kolev *et al* studied CO_2 decomposition efficiency in pulsed atmospheric gas discharge between positive and negative electrodes using a zero-dimensional (0D) plasma model [34]. This study revealed that varying pulse length and power density can enhance CO_2 dissociation and energy efficiency. Wang *et al* systematically examined the characteristics of pulsed CO_2 discharges, including product distribution and reaction pathways, within the Martian atmosphere [35]. Simulation results indicated that primary charged particles consist of electrons and CO_2^+ ions. Electron collisional dissociation and electron dissociative collisional adsorption reactions primarily generate CO and O. The characteristics of discharge and plasma chemistry are influenced by the pulsed voltage waveform and species densities rise with both the voltage rising and duration time. Kourtzanidis *et al* simulated a 2D coaxial PBDBD CO_2 plasma and determined that streamer discharge arises from a blend of glow and volumetric/surface streamers, occurring alternately and irregularly throughout the gas volume [36]. Cheng *et al* employed a 2D plasma model to study the electrodynamics, conversion rate and energy efficiency of dry reforming of methane in a nanosecond pulsed PBDBD plasma [37]. Numerical results demonstrated that plasma propagated through surface ionization waves and filamentary micro-discharges within the enclosed space between dielectric spheres. Du *et al* utilized pulsed DBD plasma to catalyze CO_2 hydrogenation and conducted numerical simulations to examine how nickel and copper catalysts affect methanol and methane selectivity [38]. The study revealed the underlying production pathways for CH_4, CH_3O and CH_3OH for each catalyst. De Bie *et al* examined the reaction mechanism of CO_2 hydrogenation in DBD plasma using a 1D fluid model, identifying primary pathways for generating CO, CH_4, CH_2O and CH_3OH under varying reaction gas ratios [39]. Liu *et al* compiled and summarized advancements in plasma CO_2 hydrogenation synthesis of valuable compounds, highlighting future research avenues [40]. Ponduri *et al* conducted numerical simulations to investigate how applied voltage affects CO_2 dissociation via DBD plasma [41]. In earlier studies, we developed 0D and 2D pin-plate models for atmospheric-pressure non-equilibrium plasma CO_2 hydrogenation, focusing on how CO_2/H_2 volume ratios affect plasma discharge characteristics [42, 43].

In summary, previous studies predominantly focused on optimizing power supply parameters, catalyst types and electrode configurations to enhance CO_2 dissociation and energy efficiency. Research on the physical mechanisms underlying plasma discharge remains relatively insufficient and scarce and requires further development. Our previous numerical simulation results indicated that the successive amount of added highly reducing H_2 can significantly alter the CO_2 plasma discharge characteristics and products. Therefore, the CO_2/H_2 molar ratio in the initial feed gas is a critical parameter that influences the discharge of products. Furthermore, there is a limited body of literature on plasma CO_2 dissociation or hydrogenation under positive and negative pulsed excitations. In this context, the present study develops a coaxial dual-layer DBD plasma fluid model for carbon dioxide hydrogenation, based on PASSKEy. This model investigates the effects of positive and negative pulsed excitation, as well as the CO_2/H_2 molar ratio, on streamer propagation, energy deposition, dielectric surface charge distribution, and discharge products. In addition, the effect of dielectric beads packing in the PBDBD reactor on plasma CO_2 hydrogenation, particularly methanol synthesis, has also been studied. The coaxial dual-layer DBD electrode structure is adopted because it can generate a stable and uniform streamer discharge with high plasma chemical activity. Moreover, the dual-layer dielectric can also protect the two metal electrodes from plasma particle erosion [44].

2. Simulation mode

2.1. Simulation configuration

This study develops a coaxial dual-layer DBD 2D fluid model using the PASSKEy (Parallel Streamer Solver with Kinetics) code. The accuracy and reliability of the numerical simulations are substantiated with relevant experimental diagnostic data, making it suitable for simulating complex reactive systems in non-thermal equilibrium plasmas [45, 46].

Figure 1(a) shows the schematic diagram of the plasma simulation's geometric structure, covering a computational area of 5×5 mm^2. As shown in figure 1(a), the central red area represents a metal high-voltage electrode (0.1 mm radius), surrounded by a tightly wrapped inner dielectric layer ($\varepsilon_r = 4$) with a thickness of 0.2 mm. The thickness of the outer dielectric layer ($\varepsilon_r = 4$) is 0.3 mm ($2.2 \leqslant R \leqslant 2.5$), and the outermost layer with a thickness of 0.01 mm serves as the grounded electrode. The blue area denotes the plasma discharge region, and the discharge gap is 1.9 mm. This electrode configuration is referred to as dual-layer DBD structure. One single positive or negative square pulsed waveform is applied to the central red electrode, as can be seen in figure 1(b). The waveform features rising and falling edges lasting 5 ns each, a peak duration of 10 ns, that is, a pulse period of 20 ns, and a peak pulse voltage of 12 kV. A numerical simulation study of the plasma CO_2 hydrogenation in PBDBD for methanol synthesis is presented in section 3.2. Specifically, the discharge gap is filled with two layers of dielectric spheres, comprising a total of 12 spheres with a radius of 0.42 mm ($\varepsilon_r = 4$). The first layer consists of six spheres arranged in a regular hexagon with a side length of 1.0 mm, and the second layer also consists of six spheres arranged in a regular hexagon with a side length of 1.73 mm.

The streamer inception and propagation in the DBD at atmospheric pressure are characterized by steep gradients of electric field and charged particles. Thus, a uniform square mesh with a size of 2.5 μm is adopted in the entire domain. Meshes are accordingly ranged up to 2000×2000 grid cells, resulting in a large computational cost, which is one of the reasons a short pulsed-dc voltage with a period of 20 ns is adopted in our model. For instance, it takes 4–7 days to complete various simulations on a DELL T7920 tower workstation, which consists of dual Intel Xeon Gold 6136 CPUs with 12 cores and 24 threads each.

2.2. Governing equations

This study employs the classical fluid model, incorporating the drift-diffusion two-term approximation of species continuity equation, the electron energy conservation equation and the Poisson equation of the electrostatic field, expressed as follows:

$$\frac{\partial n_i}{\partial t} + \nabla \cdot \boldsymbol{\Gamma}_i = S_i + S_{\mathrm{ph},i},\ i = 1, 2, \cdots, N_{\mathrm{total}}, \tag{1}$$

$$\boldsymbol{\Gamma}_i = \mu_i n_i \boldsymbol{E} - D_i \nabla n_i, \tag{2}$$

$$\frac{\partial (n_e \cdot \varepsilon_m)}{\partial t} + \nabla \cdot \boldsymbol{\Gamma}_\varepsilon = -|q_e| \cdot \boldsymbol{E} \cdot \boldsymbol{\Gamma}_e - P(\varepsilon_m), \tag{3}$$

$$\boldsymbol{\Gamma}_\varepsilon = -D_\varepsilon \nabla (n_e \cdot \varepsilon_m) - n_e \varepsilon_m \mu_\varepsilon \boldsymbol{E}. \tag{4}$$

Equation (1) defines n_i as the number density of each ith species, with S_i and S_{ph} representing chemical reaction and photoionization terms, μ_i and D_i denoting the mobility and diffusion coefficients of charged species, respectively. $\boldsymbol{E}$ signifies the electric field, while $\boldsymbol{\Gamma}_i$ stands for the flux of species (equation (2)). Our model excludes the photoionization effect of CO_2 because no efficient photoionization mechanism is known for gases with a large CO_2 fraction since photons in the relevant energy range are quickly absorbed [46]. Equations (3) and (4) define variables n_e, ε_m, $\boldsymbol{\Gamma}_e$, $\boldsymbol{E}$, q_e, D_ε, μ_ε and $P(\varepsilon_m)$ as electron number density, mean electron energy, electron energy flux, electric field, elementary charge, electron energy diffusion coefficient, mobility, and electron collision power lost, respectively [47]. In equation (3), the first and second terms on the right-hand side represent the energy gained by the accelerated electrons in response to the electric field and the energy consumed by the electron collision reactions, respectively. Local Mean Energy Approximation (LMEA) and Local Field Approximation (LFA), which are commonly used for transport, rate coefficients and other electronic properties, are included in the hydrodynamic description of gas discharge plasma. Research indicates that LMEA is more accurate and reliable when the steamer contacts the dielectric surface at both the head and bottom [48, 49]. Therefore, in this study, electron swarm parameters including electron transport coefficients, reaction rates and electron collision power lost are calcu-

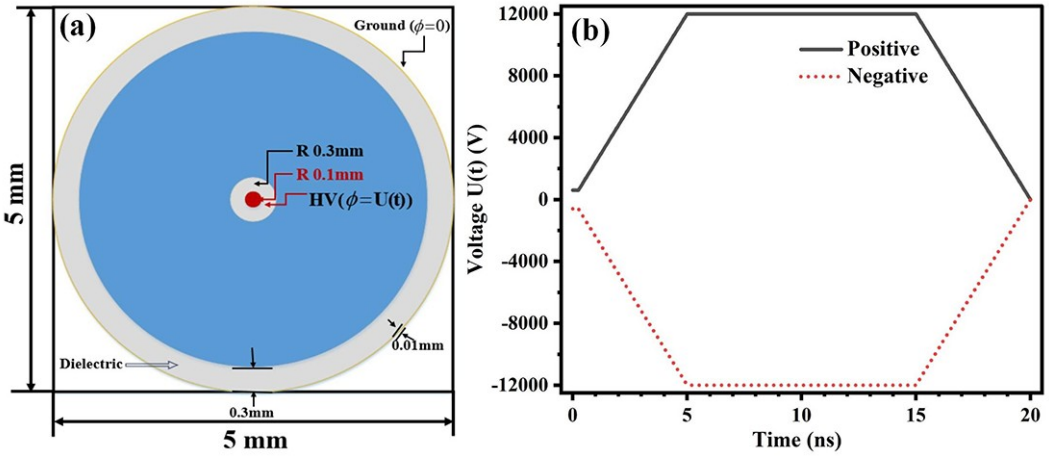

Figure 1. (a) Simulation configuration and (b) positive and negative nanosecond pulsed voltage waveforms.

lated by Bolsig+ using the LMEA method [50].

The Poisson equation takes into account the surface charge density over the dielectric:

$$\nabla(\varepsilon_0\varepsilon_r\nabla\phi) = -\rho - \sigma, \tag{5}$$

$$\frac{\partial\sigma}{\partial t} = \sum_i q_i(-\nabla\cdot\boldsymbol{\Gamma}_i), \tag{6}$$

where ρ is the space charge density, σ is the surface charge density on the dielectric and ϕ is the electric potential. ε_0 and ε_r are the dielectric constant in vacuum and the relative dielectric constant of dielectric material ($\varepsilon_r = 4$), respectively. To facilitate calculations, a simplified CO_2/H_2 chemical reaction fluid model is used. The CO_2/H_2 kinetic scheme includes 22 species and 52 chemical reactions, as shown in tables 1 and 2, respectively. Detailed plasma chemical reactions include 12 electron collision reactions and 40 reactions involving heavy particles.

2.3. Initial and boundary conditions

For the initial conditions, all the simulations are carried out in the homogeneous CO_2/H_2 mixtures (4:1, 2:1 and 1:1) at 300 K and atmospheric pressure. The initial seed electron density is 10^{10} m^{-3} uniformly distributed in the plasma domain, and the same initial ion density is obtained based on quasi-neutrality. For the Poisson equation, classical Dirichlet boundary conditions are applied on metal surfaces, including the central metal electrode $\phi = \pm U(t)$ and outermost grounded electrode $\phi = 0$, while Neumann boundary conditions are used on the non-metal boundary: $\partial\phi/\partial n = 0$. For the transport equation, simple flux continuity boundary conditions are taken into account. A zero-flux boundary condition is applied at plasma-surface interfaces for neutral species. For charged species, incoming electrons at the boundary are represented as $\partial\boldsymbol{\Gamma}_e/\partial n = 0$, and outgoing electrons as $\boldsymbol{\Gamma}_e = -\gamma\boldsymbol{\Gamma}_i$. Incoming ions at the boundary are represented as $\partial\boldsymbol{\Gamma}_i/\partial n = 0$, and outgoing ions as $\boldsymbol{\Gamma}_i = 0$. The model assumes a secondary emission coefficient of $\gamma = 0.01$ for dielectric. It is worth noting that the use of plasma boundary conditions in this way has defects, and is therefore not suitable for accurately calculating the plasma sheath at the boundary. Typically, the Neumann boundary condition is a simpler solution. However, due to the fact that determining the electric field at the model boundary and specifying plasma density values at virtual grid points are inconsistent with the model algorithm (explicit, operator splitting), earlier studies have adopted a compromise flux continuity boundary [32, 57]. Although this boundary is not perfect, it is adequate for the purpose of the streamer propagation simulation in this study. The comparisons between earlier papers and experimental results also confirm this point [32].

Table 1. Overview of particles included in the model.

Item	Particle
Molecule	CO_2, H_2, H_2O, CO, O_2, CH_3OH
Ion	CO_2^+, H_2^+, CO^+, O_2^+, H_2O^+, O^-
Radical	C, H, OH, CH, CH_2, CH_3, CHO, CH_3O, CH_2OH

3. Results and discussion

3.1. Coaxial dual-layer DBD plasma propagation stage

Figures 2(a)–(c) show the spatiotemporal distributions of electron density in positive pulsed streamer with CO_2/H_2 volume ratios of 4:1, 2:1 and 1:1, respectively. Figure 2(d) shows the spatiotemporal distribution of electron density in negative pulsed streamer with a CO_2/H_2 volume ratio of 2:1. Obviously, the positive pulse excitation produces a cathode-directed positive streamer, which glows at the surface of the inner dielectric layer at about 4 ns, and the streamer channel spreads to the outer grounded dielectric layer as the voltage increases. The PASSKEy software employs a uniform square grid to discretize the circular dielectric layers, which results in small protrusions at four symmetric directions on the dielectric sphere surface, leading to geometric curvature discontinuity. These protrusion regions induce the local electric field enhancements. When the applied voltage reaches the breakdown threshold, the streamer preferentially initiates and propagates from these micro-protrusions, resulting in the formation of these branching streamers. It is noteworthy that when the grid cell size is reduced from 4.0 μm to 2.5 μm, the grid division at these micro-protrusion locations becomes smoother, which largely suppresses the extent of streamer branching (data not shown). However, even with finer grid division, this branching phenomenon cannot be eliminated, at the cost of significantly increased computational burden. Therefore, based on the inherent limitations of the model grid division and the trade-off in computational efficiency, the grid size in this study is set to a moderate 4.0 μm. However, as the dielectric spheres are filled in PBDBD, it seems that the positive streamer propagates through the gaps between the adjacent inner dielectric spheres. In addition, positive streamers also exhibit multi-directional propagation rather than uniform expansion in PBDBD. It is noteworthy that the morphology of streamer propagation exhibits substantial variation depending on the initial hydrogen concentration increase from 20% to 50%. The streamer discharge channels tend to shrink more and to propagate faster, which is consistent with experimental observations in Liu *et al* [58]. This phenomenon may be attributed to the fact that the ionization rates are elevated due to the increasing energy deposition with high initial H_2 content. Unlike positive streamer, the discharge channel of negative streamer is more uniformly dispersed, with no distinct streamer head. The discharge channel fills the entire discharge space, which is consistent with the basic characteristics of negative streamer, as shown in figure 2(d).

As shown in figures 2(e) and (f), the spatiotemporal distributions of electron density in the PBDBD positive streamer are shown with CO_2/H_2 volume ratios of 2:1 and 1:1, respectively. It can be observed that the positive

Table 2. Chemical reactions included in our model (molecules-meters-Kelvin).

Index	Reaction formula[a]	Rate constant[b]	Threshold (eV)	Reference
R1	$e + H_2 => e + 2H$	$f(\varepsilon_m)$	8.9	[51]
R2	$e + H_2 => 2e + H_2^+$	$f(\varepsilon_m)$	15.4	[51]
R3	$e + CO_2 => 2e + CO_2^+$	$f(\varepsilon_m)$	13.8	[52]
R4	$e + CO_2 => CO + O^-$	$f(\varepsilon_m)$		[52]
R5	$e + CO_2 => 2e + CO^+ + O$	$f(\varepsilon_m)$	19.5	[53]
R6	$e + CO => 2e + CO^+$	$f(\varepsilon_m)$	14	[51]
R7	$e + CO => C + CO^-$	$f(\varepsilon_m)$		[51]
R8	$e + O_2 => O + O^-$	$f(\varepsilon_m)$		[51]
R9	$e + O_2 => 2e + O_2^+$	$f(\varepsilon_m)$	12.06	[51]
R10	$e + H_2O => H_2 + O^-$	$f(\varepsilon_m)$		[52]
R11	$e + H_2O => e + H + OH$	$f(\varepsilon_m)$	7	[52]
R12	$e + H_2O => 2e + H_2O^+$	$f(\varepsilon_m)$	13	[52]
R13	$e + H_2^+ => 2H$	1.6×10^{-14}		[56]
R14	$e + CO_2^+ => C + O_2$	$3.94\times10^{-13}T_e^{-0.4}$		[54]
R15	$e + CO_2^+ => CO + O$	$2\times10^{-11}T_e^{-0.5}$		[54]
R16	$e + CO^+ => C + O$	$3.68\times10^{-14}T_e^{-0.55}$		[54]
R17	$e + O_2^+ => O + O$	$6\times10^{-13}T_e^{-0.5}T_g^{-0.5}$		[54]
R18	$e + H_2O^+ => H + OH$	$5.1\times10^{-14}T_e^{-0.5}$		[55]
R19	$H + H + M => H_2 + M$	6×10^{-45}		[56]
R20	$H + CO + M => CHO + M$	1.54×10^{-46}		[56]
R21	$H + OH + M => H_2O + M$	4.33×10^{-42}		[56]
R22	$O + CO + M => CO_2 + M$	1.11×10^{-47}		[56]
R23	$O + CHO => H + CO_2$	5×10^{-17}		[56]
R24	$O + CHO => CO + OH$	5×10^{-17}		[56]
R25	$CH_3O + H => CH_3OH$	$3.39\times10^{16}\times(T_g/29)^3$		[55]
R26	$O + O + M => O_2 + M$	7.19×10^{-45}		[56]
R27	$H + CH_3OH => CH_3O + H_2$	3.18×10^{-22}		[56]
R28	$CH_3 + OH + M => CH_3OH + M$	2.3×10^{-39}		[56]
R29	$H_2O + CH_3O => CH_3OH + OH$	1.67×10^{-29}		[56]
R30	$CHO + CH_3O => CH_3OH + CO$	1.5×10^{-16}		[56]
R31	$H_2 + CH_2OH => CH_3OH + H$	1.89×10^{-29}		[56]
R32	$H + CH_2OH + M => CH_3OH + M$	1.18×10^{-41}		[56]
R33	$O + CH_3OH => OH + CH_2OH$	1.12×10^{-20}		[56]
R34	$O + CH_3OH => OH + CH_3O$	1.68×10^{-21}		[56]
R35	$OH + CH_3OH => H_2O + CH_2OH$	7.67×10^{-19}		[56]
R36	$OH + CH_3OH => H_2O + CH_3O$	1.35×10^{-19}		[56]
R37	$CHO + CH_2OH => CH_3OH + CO$	2×10^{-16}		[56]
R38	$C + H_2 => CH + H$	1.5×10^{-16}		[56]
R39	$CH + H_2 => CH_2 + H$	6.8×10^{-19}		[56]
R40	$CH + CO_2 => 2CO + H$	9.68×10^{-19}		[56]
R41	$CH + CO_2 => 2CO + H$	9.68×10^{-19}		[56]
R42	$CH + O => CO + H$	6.6×10^{-17}		[56]
R43	$CH_2 + H_2 => CH_3 + H$	5×10^{-21}		[56]
R44	$CH + O_2 => CHO + O$	8×10^{-18}		[56]
R45	$C + O_2 => CO + O$	2.45×10^{-19}		[56]
R46	$O^- + H_2 => H_2O + e$	7×10^{-16}		[56]
R47	$O^- + CO => CO_2 + e$	6.5×10^{-16}		[56]
R48	$O^- + O => O_2 + e$	2.3×10^{-16}		[56]
R49	$O^- + H => OH + e$	5×10^{-16}		[56]
R50	$H_2O^+ + O_2 => O_2^+ + H_2O$	4.6×10^{-16}		[56]
R51	$CO^+ + O_2 => CO + O_2^+$	1.2×10^{-16}		[56]
R52	$CO^+ + CO_2 => CO_2^+ + CO$	1×10^{-15}		[56]

[a]M represents the background gases CO_2 and H_2 molecule.

[b]Rate coefficients of two- and three-body reactions have units of m^3/s and m^6/s, respectively. T_e (electron temperature) has the unit of eV and T_g has the unit of K. $f(\varepsilon_m)$ represents the rate constant as a function of mean electron energy ε_m.

streamer begins to glow in the inner dielectric layer at 3 ns, and as the voltage increases, the streamer propagation becomes primarily concentrated in the gaps between the dielectric spheres. This phenomenon mainly results from the

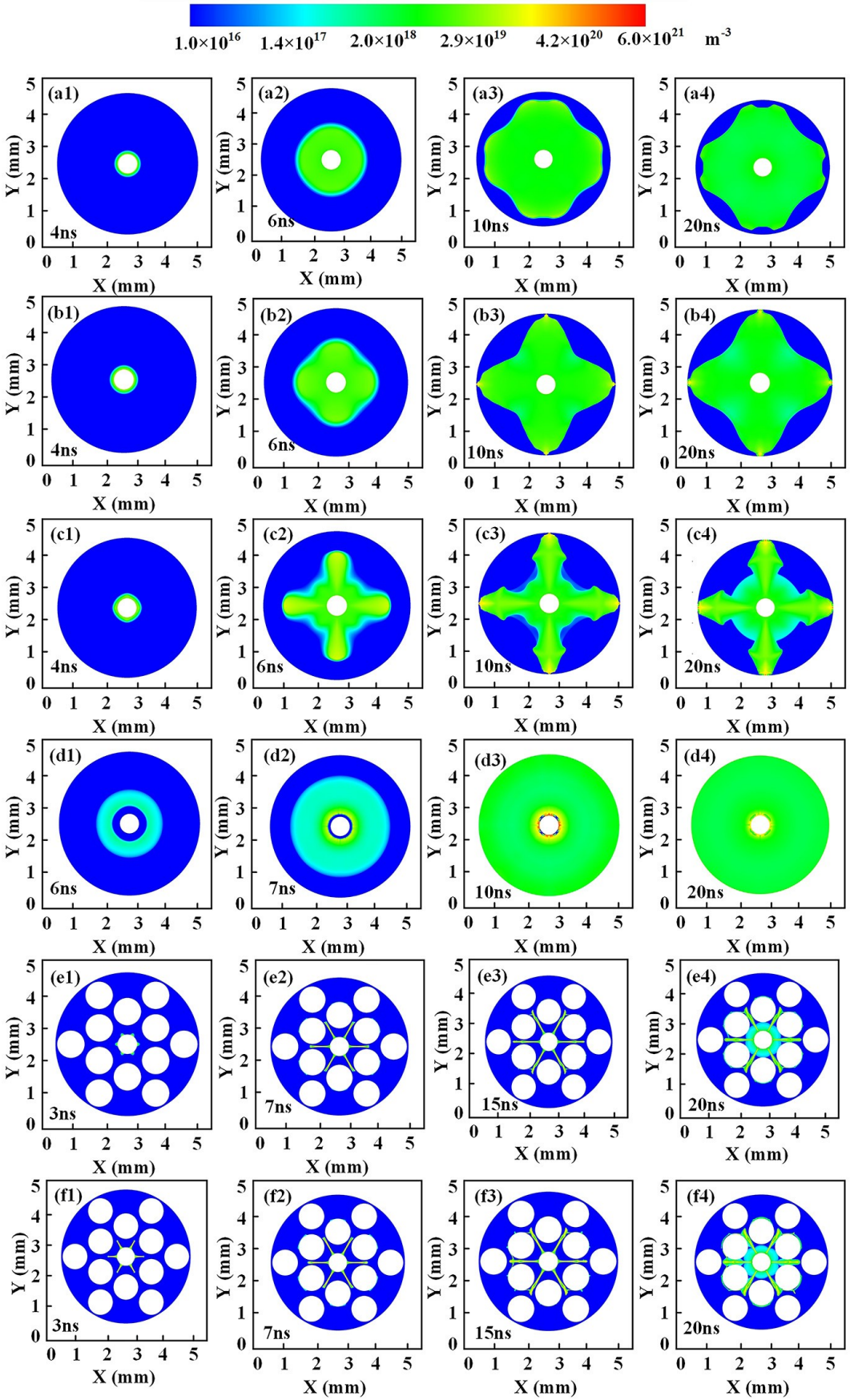

Figure 2. (a)–(c) Spatiotemporal distributions of electron density for positive streamers with CO_2/H_2 volume ratios of 4:1, 2:1 and 1:1, (d) negative streamers with CO_2/H_2 volume ratio of 2:1, (e) and (f) PBDBD positive streamer for CO_2:H_2 = 2:1 and CO_2:H_2 = 1:1, respectively.

polarization of dielectric spheres in the electric field, which leads to the accumulation of bound charges within the dielectric and the formation of localized strong electric fields near the surface. Although the enhanced surface electric field promotes charge accumulation, it simultaneously restricts the lateral propagation of streamer along the dielectric surface [59]. When the voltage reaches its peak value, FMs start to form within the gaps. As the electron density continues to rise at 15 ns, surface ionization waves (SIWs) appear on the surface of the inner dielectric spheres, forming the SIWs and FMs structure (figures 2(e3) and (f3)). This delayed appearance occurs because the initial strong polarization confines the plasma to the gas gaps, while the subsequent voltage reduction allows residual charges to redistribute along the dielectric surface, thereby enabling SIW formation. Obviously, due to the filling of the dielectric spheres, the streamers only advance to the region between the inner and outer dielectric spheres. This also indicates that the propagation speed of streamers in the PBDBD is slower than that in the DBD (shown in figure 2).

As shown in figures 3(a)–(c), during the propagation stage of the positive streamer, the electric field distribution is extremely non-uniform. A reduced electric field of hundreds of Td is formed at the streamer head due to the accumulation of a large amount of positive charge at the streamer head. This induces a strong local electric field, and the spatial electric field distribution of the streamer body is relatively uniform, which is a typical characteristic of positive streamer [49]. Furthermore, with an increase in initial hydrogen content, the reduced electric field also shows a more constrained and contracted spatial distribution, and the head of the streamer propagates faster. The spatial distributions of the reduced electric field are in good agreement with the electron density distributions shown in figure 2. As shown in figure 3(d), the spatial reduced electric field distribution of the negative pulsed streamer is relatively uniform, resulting in the discharge streamer dispersing uniformly throughout the entire space without a distinct bright head feature. Furthermore, compared to positive streamer, a locally strong reduced electric field forms near the surface of the inner dielectric layer, due to the accumulation of numerous positive charges on the surface of the inner dielectric layer.

Figure 4 shows the spatial distributions of the electron temperature at 10 ns. As can be seen, high-energy electrons are mainly concentrated at the head of the streamer, while the electron temperature of the streamer body is relatively low, generally 1–2 eV. In contrast, for the negative streamer, high-energy electrons are mainly concentrated near the surface of the inner dielectric layer, as shown in figure 4(d). Figure 5 shows the temporal evolutions of the peak electron density and temperature at the head of the streamer. The observed trend is that with an increase in the initial hydrogen content, the

peak values of electron density and electron temperature at the streamer head are higher. This is consistent with our previous zero-dimensional fluid model results and related microwave plasma emission spectroscopy diagnostic data [26, 42]. In fact, as the initial hydrogen content increases, the density of H atoms generated by electron collision dissociation is higher. On one hand, H atoms (13.6 eV) have a lower ionization threshold energy compared to CO_2 molecules. On the other hand, H atoms do not have vibrational and rotational states, leading to higher electron energy and ionization rates. Consequently, the spatial charge density accumu-

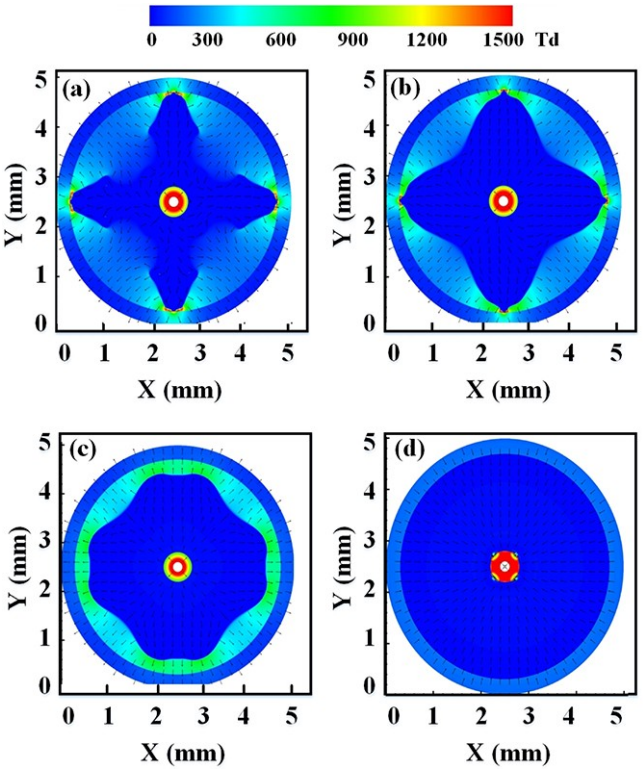

Figure 3. (a)–(c) Spatial distributions of reduced electric field for positive pulsed streamers with CO_2/H_2 = 4:1, 2:1 and 1:1, and (d) negative pulsed streamers with CO_2/H_2 = 2:1 at 10 ns.

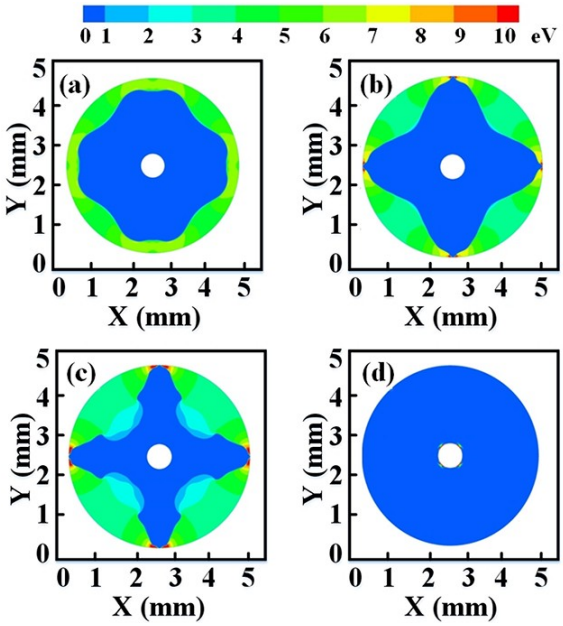

Figure 4. (a)–(c) Spatial distributions of electron temperature for positive pulsed streamers with CO_2/H_2 = 4:1, 2:1 and 1:1, and (d) negative pulsed streamers with CO_2/H_2 2:1 at 10 ns.

lated at the streamer head is higher, the head of the streamer propagates faster (as shown in figure 6), and the peak values of electron temperature and electron density are also higher.

Figure 6 shows the variations of the streamer propagation distance and velocity over time. It is evident that for positive streamers, the propagation velocity increases with higher hydrogen content. It is commonly accepted that the propagation speed of the streamer correlates with the accumulated space charge at its head and the charge deposition on the dielectric surface. It is worth mentioning that the propagation speed of the negative streamer is slightly higher than that of the positive streamer in atmospheric CO_2/H_2 plasma, as shown in figure 6. In contrast, for the streamer dynamic in atmospheric air, positive streamer propagates significantly faster than negative streamer [51]. However, in CO_2 plasma at ambient temperature in the pressure range of 0.05–0.5 MPa, experimental results demonstrated that negative streamer is faster than positive streamer [60], which is generally consistent with simulation results in our model.

3.2. The spatiotemporal development of major radicals and ions

Figure 7 shows the spatial density distributions of the main radicals CO, O and H in the positive and negative streamers with CO_2/H_2 = 2:1 at 10 ns, respectively. The peak densities of three radicals produced by the positive streamer are 1.67×10^{22} m^{-3}, 1.65×10^{22} m^{-3} and 1.73×10^{22} m^{-3}, respectively, whereas those produced by the negative streamer are 8.87×10^{21} m^{-3}, 8.80×10^{21} m^{-3} and 5.13×10^{21} m^{-3}, differing by nearly an order of magnitude. Furthermore, as shown in figures 7(a)–(c), the spatial distributions of radical densities produced by positive streamers show a non-uniform pattern, with higher densities at the streamer head, while the radical density distributions for negative streamers are more uniform, which is also due to the characteristics between positive and negative streamers. Comparing figures 2 and 7, it is evident that the spatial density distributions of the three main radicals are similar to the electron density distributions, indicating that the three main radicals produced by the positive and negative streamer discharges are generated by electron collision ionization/dissociation of feed gas molecules, which is consistent with our previous numerical simulation results [42].

Figure 8 shows the spatial density distributions of dominant cations CO_2^+, H_2^+ and CO^+ in the positive and negative streamers with CO_2/H_2 = 2:1 at 10 ns, respectively. For the positive streamer discharge, the peak densities of CO_2^+, H_2^+ and CO^+ ions are 2.76×10^{21} m^{-3}, 2.58×10^{21} m^{-3} and 1.25×10^{20} m^{-3}, respectively, whereas for negative streamers, they are 2.4×10^{21} m^{-3}, 1.58×10^{21} m^{-3} and 1.09×10^{20} m^{-3}, respectively. It is evident that CO_2^+ and H_2^+ exhibit a non-uniform

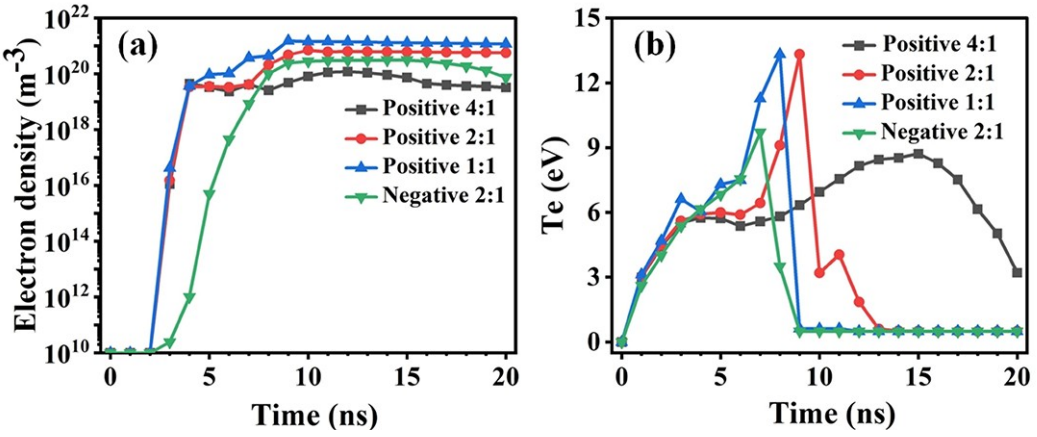

Figure 5. Temporal evolutions of (a) the peak electron density and (b) electron temperature at the head of the streamer.

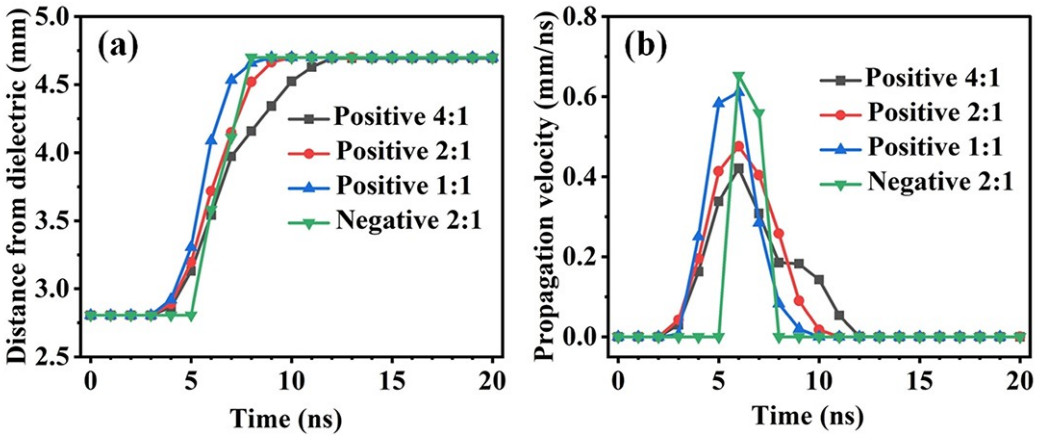

Figure 6. Variations of (a) the streamer propagation distance and (b) velocity over time.

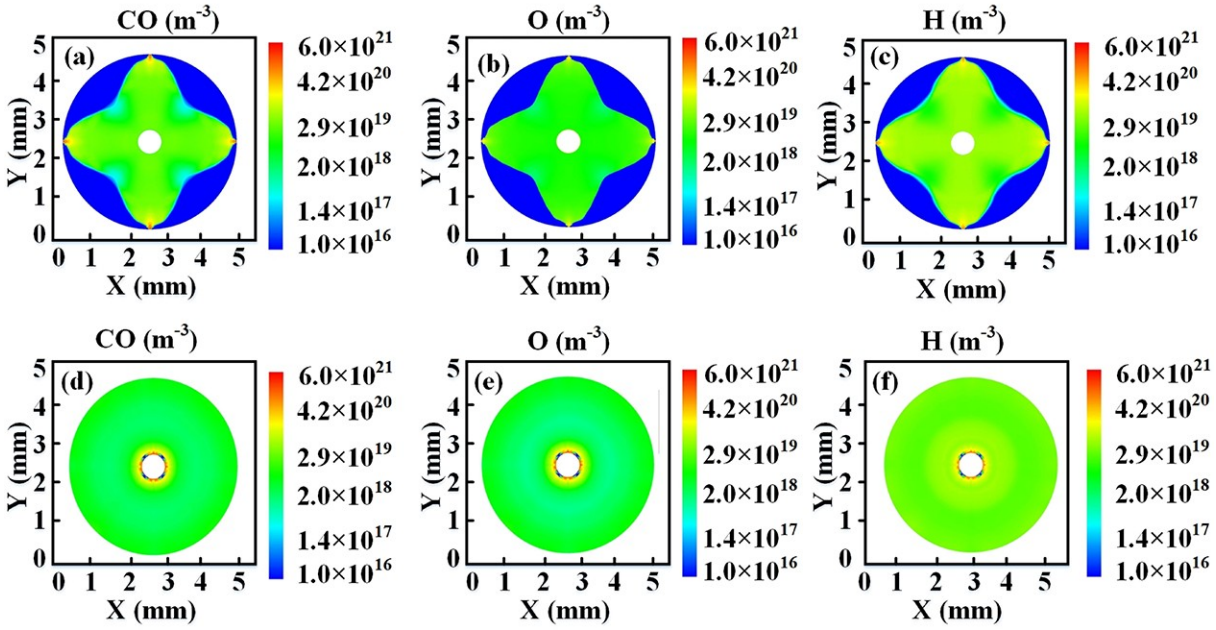

Figure 7. (a)–(c) Spatial density distributions of the main radicals CO, O and H in the positive and (d)–(f) negative streamers with CO_2/H_2 = 2:1 at 10 ns.

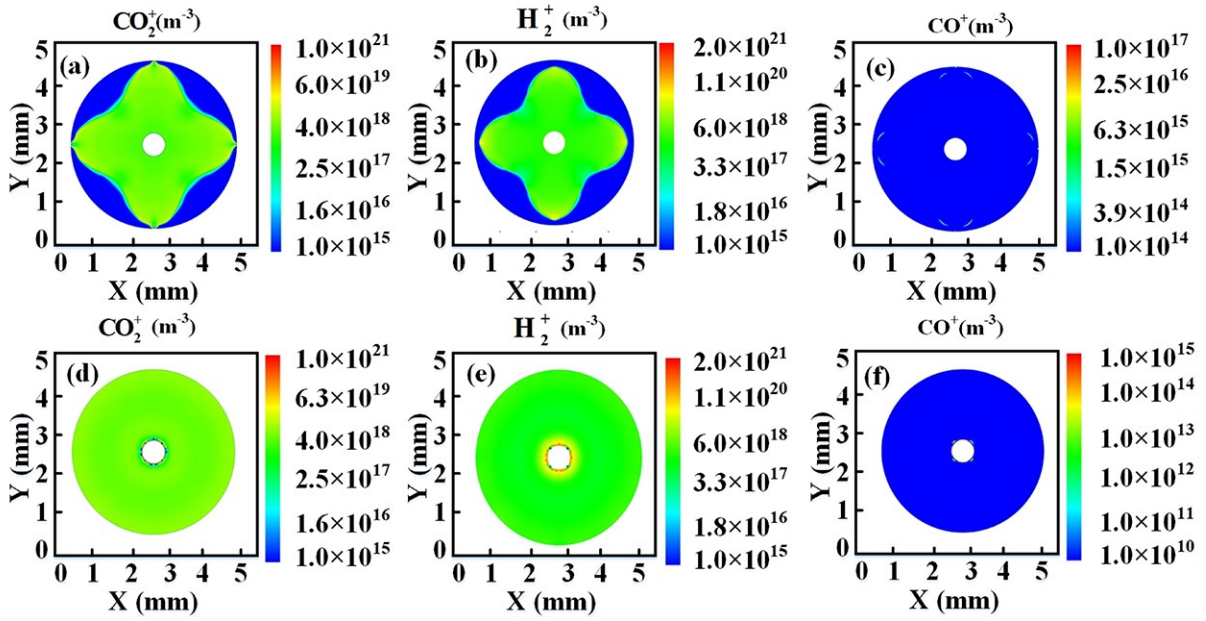

Figure 8. (a)–(c) Spatial density distributions of dominant cations CO_2^+, H_2^+ and CO^+ in the positive and (d)–(f) negative streamers with CO_2/H_2 = 2:1 at 10 ns.

spatial density distribution similar to that of electron density, while CO^+ is only concentrated at the streamer head or the surface of the inner layer with a lower density, as shown in figure 8. This is primarily due to the production reactions of these cations and the characteristics of positive and negative streamer discharges. The main reaction pathways to produce CO^+ are $e + CO_2 => O + CO^+ + e + e$ and $e + CO => CO^+ + e + e$, with ionization threshold energies of 19.1 eV and 14.01 eV, respectively. These are much higher than the ionization threshold energies for collisions between electrons and carbon dioxide (13.7 eV) or hydrogen molecules (15.4 eV) This means that only high-energy electrons in the localized strong electric field regions at the streamer head or the front of the ionization wave can ionize CO molecules to form CO^+. In addition, the main cations produced by positive streamer discharge also exhibit a non-uniform spatial distribution, while the cations produced by negative streamer are more uniformly dispersed. This is consistent with the spatial distributions of electron density in positive and negative streamers, as shown in figure 2, and suggests that these dominant cations are mainly generated by direct electron-impact ionization reactions of CO_2/H_2 molecules.

Figure 9 shows spatial distributions of energy density for positive and negative streamers with CO_2/H_2 = 4:1, 2:1 and

1:1 at 20 ns. It is evident that the spatial distribution of energy density exhibits a pattern similar to that of electron density, as depicted in figure 2. Specifically, as the H_2 content in the reactant gas increases, the energy density distribution of the positive streamer becomes more concentrated, while the energy density in the negative streamer is more uniformly dispersed throughout the discharge gap. By calculating the product of energy density and volume per cell unit and summing over the plasma discharge region, the total energy deposition can be obtained, as shown in figure 10. The primary sources of energy deposition in both positive and negative streamers are electrons. As the initial hydrogen content increases, the energy deposition by electrons and CO_2^+ ions in the positive streamer slightly decreases, while the energy deposition by H_2^+ ions slightly increases. However, the total energy deposition is not very sensitive to the variation of initial hydrogen content. It is worth noting

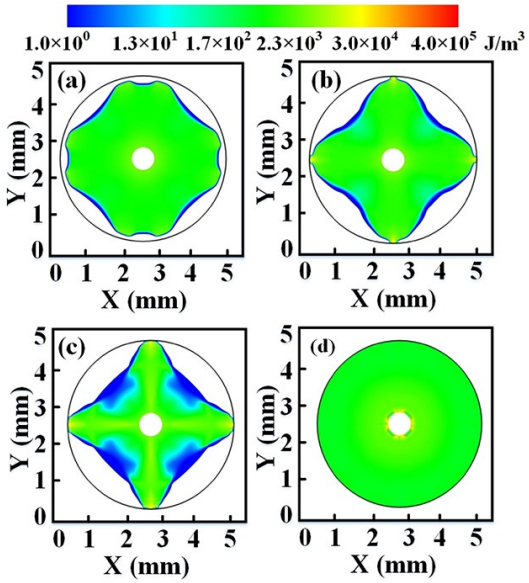

Figure 9. Spatial distributions of energy density for positive streamer with CO_2/H_2 = (a) 4:1, (b) 2:1, (c) 1:1 and (d) negative streamer with CO_2/H_2 = 2:1 at 20 ns.

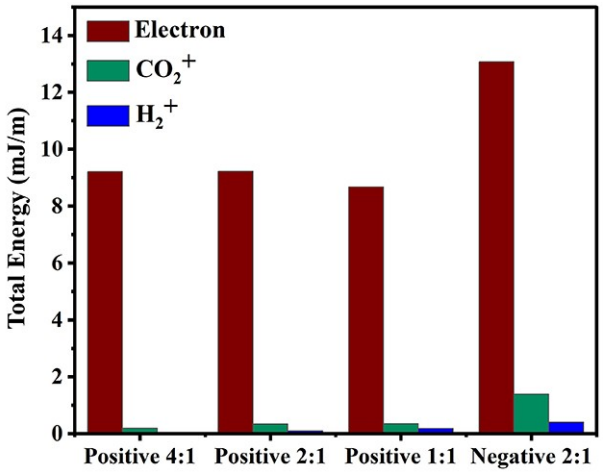

Figure 10. Proportion of total energy deposited in positive and negative streamers related to electrons, CO_2^+ and H_2^+ for three volume ratios of CO_2/H_2.

that the energy deposition by electrons, CO_2^+ and H_2^+ in the negative streamer is significantly higher than that in the positive streamer. The difference in energy deposition between the positive and negative streamers may be due to two factors. First, pre-ionized seed electrons instead of photoionization are used in our model, without considering the effects of photoionization. Generally, positive streamer requires photoionization effect to generate seed electrons to compensate for the rapid loss of electrons, while the photoionization effect is negligible in negative streamer [61].

Although reference [46] emphasized that no efficient photoionization mechanism is known for gases with a large CO_2 fraction, it is undeniable that photoionization is crucial for positive streamer in CO_2, which may contribute to the lower energy deposition calculated for positive streamer. Second, compared to the contraction and concentration of the discharge channel in positive streamer, the negative streamer discharge channel is more uniformly dispersed throughout the entire discharge gap, leading to higher energy deposition in negative streamer.

Figure 11 shows the spatial density distributions of methanol generated by positive streamer DBDs with three volume ratios of CO_2/H_2 (figures 11(a)–(c)), negative streamer DBD with volume ratio of CO_2/H_2 = 2:1 (figure 11(d)) and positive streamer PBDBDs with two volume ratios CO_2/H_2 = 2:1 and 1:1 (figures 11(e) and (f)), at the end of the voltage pulse (20 ns), respectively. Clearly, as the initial hydrogen content increases, the methanol density in the positive streamer discharge becomes higher and more diffuse. Generally, this is consistent with the chemical gas chromatography diagnostic data from Wang *et al* [31], indicating that an increase in the initial hydrogen content is beneficial for the synthesis of methanol molecules. As shown in table 2, methanol generation reactions include R25, R28–R32, and R36, with the main pathway being R25: $CH_3O + H => CH_3OH$ [43]. As the initial H_2 content increases, the densities of intermediate species such as H atoms, CHO, CH_2O and CH_3O involved in methanol synthesis also rise, and the reaction rates for methanol synthesis from these intermediate species increase rapidly. In contrast, the methanol produced by negative streamer discharge is primarily concentrated on the surface of the inner dielectric layer. Furthermore, the propagation speed of streamer in PBDBD is significantly slowed down, and methanol is primarily concentrated inside the inner dielectric spheres at the end of the voltage pulse (20 ns), as shown in figures 11(e) and (f). Figure 12(a) displays the 1D density distribution of methanol at y = 2.5 mm in the positive DBD, negative DBD, and positive PBDBD streamer discharges with three volume ratios of CO_2/H_2. It is worth noting that due to the filling of the dielectric spheres, the 1D radial distribution of methanol in the PBDBD extends only up to x = 3.7 mm. Obviously, methanol molecules generated by positive streamer discharges are primarily concentrated near the outer dielectric layer (close to the streamer head), especially for the low hydrogen content. However, methanol molecules generated by negative streamer discharge are mainly concentrated near the surface of the inner dielectric layer. Due to

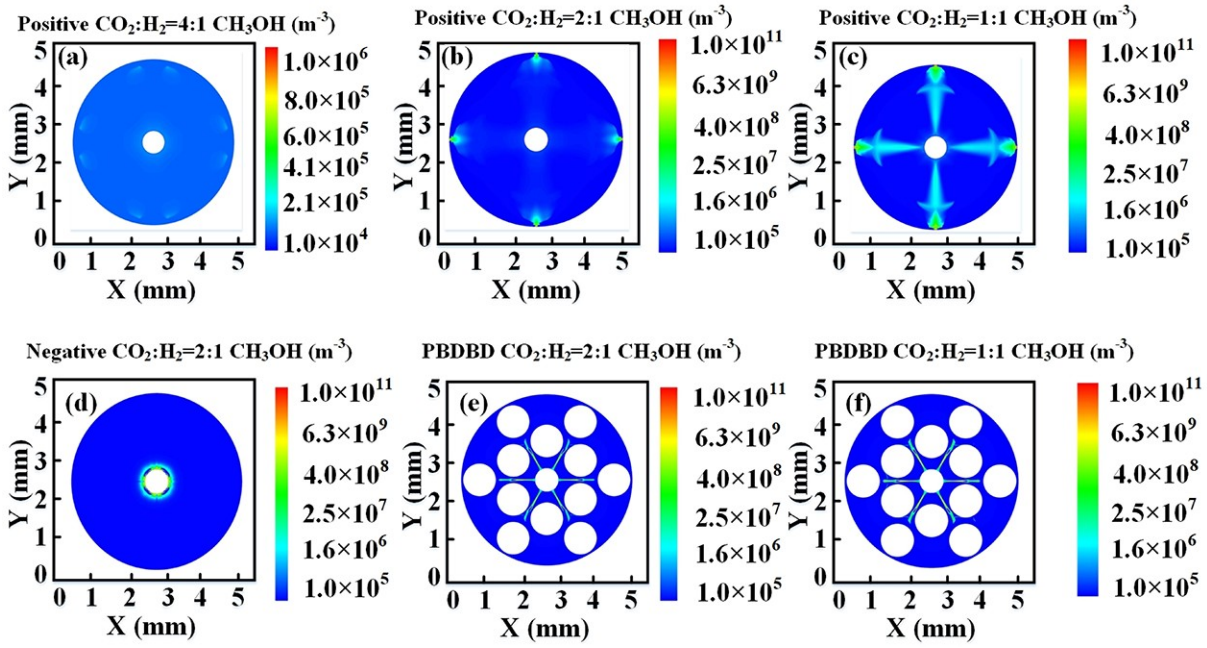

Figure 11. Spatial density distributions of CH_3OH for DBD positive streamers with CO_2/H_2 = (a) 4:1, (b) 2:1, (c) 1:1, (d) negative streamers with CO_2/H_2 = 2:1 at 20 ns, PBDBD positive streamers with CO_2/H_2 = (e) 2:1 and (f) 1:1 at the end of the voltage pulse (20 ns).

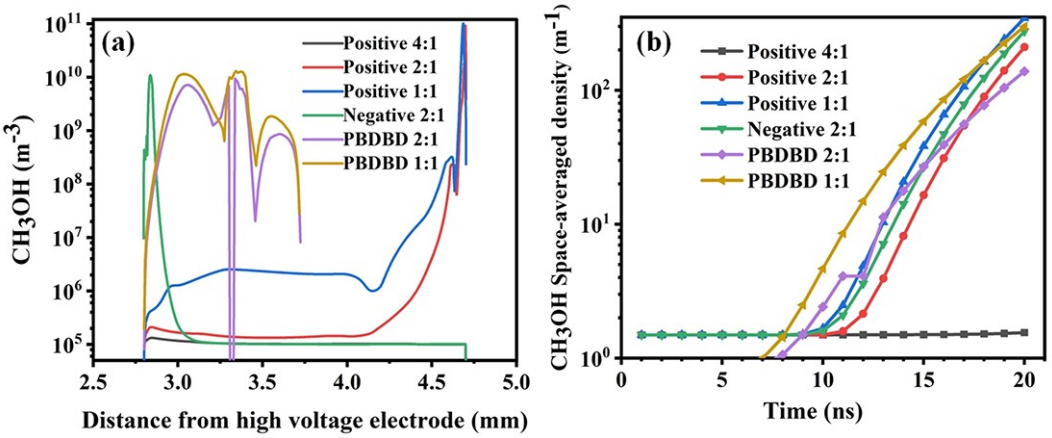

Figure 12. (a) 1D spatial density distributions of methanol along the discharge gap for y = 2.5 mm and (b) the variation of space-averaged densities of methanol with time.

the filling of dielectric spheres, although the methanol produced by PBDBD is confined to inner dielectric spheres (x = 2.8–3.7 mm), its density is much higher than that of the DBD without dielectric sphere filling. This may be attributed to local electric field enhancement induced by the polarization of the dielectric spheres. Furthermore, as the initial hydrogen content increases from CO_2/H_2 = 2:1 to 1:1, the methanol density along the 1D radial distribution in PBDBD is also higher, which is consistent with the situation in DBD. Figure 12(b) presents the variation of integrated space-averaged density of methanol with time, further illustrating that an increase in hydrogen content favors the synthesis of methanol molecules. The total energy deposited in negative streamers is larger than that in positive streamers (shown in figure 10), which is responsible for the higher space-averaged density of methanol in negative streamer discharge compared to positive streamer discharges. In addition, when the excitation voltage is a short pulse (i.e. 20 ns in our model), since the streamer in PBDBD is confined to inner dielectric spheres and has not bridged the discharge gap at the end of the voltage pulse (20 ns), the space-averaged density of methanol produced by PBDBD is significantly higher than that by DBD, except when the streamer head of DBD gradually approaches the grounded dielectric later (shown in figure 12(b)). However, when the voltage pulse period is increased to 30 ns, the streamer bridges the entire discharge gap, and the space-averaged density of methanol produced by PBDBD increases significantly (data not shown). It should be pointed out that the catalyst dielectric bead in PBDBD is only considered as a dielectric, and the surface reactions on the catalyst are not taken into account in our model, which may be far from the actual catalytic reaction.

In atmospheric-pressure DBD discharge, the surface charge deposited on the dielectric surface plays a crucial role in the discharge evolution. For example, the endogenous electric field can oppose the applied electric field, prevent-

ing the rapid increase in current. Figure 13(a) shows the polar coordinates with the center of the high-voltage electrode as the origin, where the top, middle and bottom of the inner dielectric layer are represented by polar angles $\theta = 90°$, 0° and −90°, respectively. The 2D spatiotemporal distributions of charge deposited on the dielectric surface during positive streamer discharge for three different volume ratios are shown in figures 13(b)–(d). It can be seen that the polarity of the charge deposited on the inner dielectric surface is opposite to the polarity of the voltage applied to the central metal electrode, that is, during positive streamer discharge, negative surface charge is deposited, while during negative streamer discharge, positive surface charge is deposited (see figure 13(e)). During positive streamer discharge, within the first 3 ns, the voltage is insufficient to cause breakdown, and the negative charge deposited on the dielectric surface is also low (below 10^{-10} C/m^2). As the applied voltage increases further and reaches the breakdown voltage, the electron avalanche generates numerous positive and negative space charges. As the space charges rapidly respond to the electric field and continuously accumulate on the surface of the dielectric, the resulting endogenous electric field strengthens, thereby counteracting the applied electric field. Then, the surface charge density remains roughly constant at its peak value until the secondary reverse discharge occurs. As shown in figures 13(b)–(d), as the initial hydrogen content increases from 20% to 50%, the surface charge density reaches a higher peak at an earlier stage, from -1.1×10^{-3} C/m^2 to -1.24×10^{-3} C/m^2. This indicates that higher initial hydrogen contents lead to higher discharge ionization rates and faster streamer propagation. Notably, the 2D spatiotemporal distribution of positive charge deposited on the inner dielectric surface during negative streamer discharge exhibits distinct patterns correlated with discharge development stages. Figure 13(e) shows a peak density of surface charge as high as 1.9×10^{-3} C/m^2, which is higher than that during positive streamer discharge. A comprehensive comparison of positive and negative streamer propagation speed (figure 6), total energy deposition (figure 10) and surface charge density distribution (figure 13) leads to the conclusion that the total energy deposited during negative streamer discharge is higher, causing the surface charge density to also be higher, and the streamer is faster. The negative streamer discharge is more diffuse and uniform, which results in more uniform spatial distributions of reduced electric field and generated active particles. In contrast, positive streamer discharge is more concentrated, with a local high electric field at the streamer head, leading to a steeper spatial

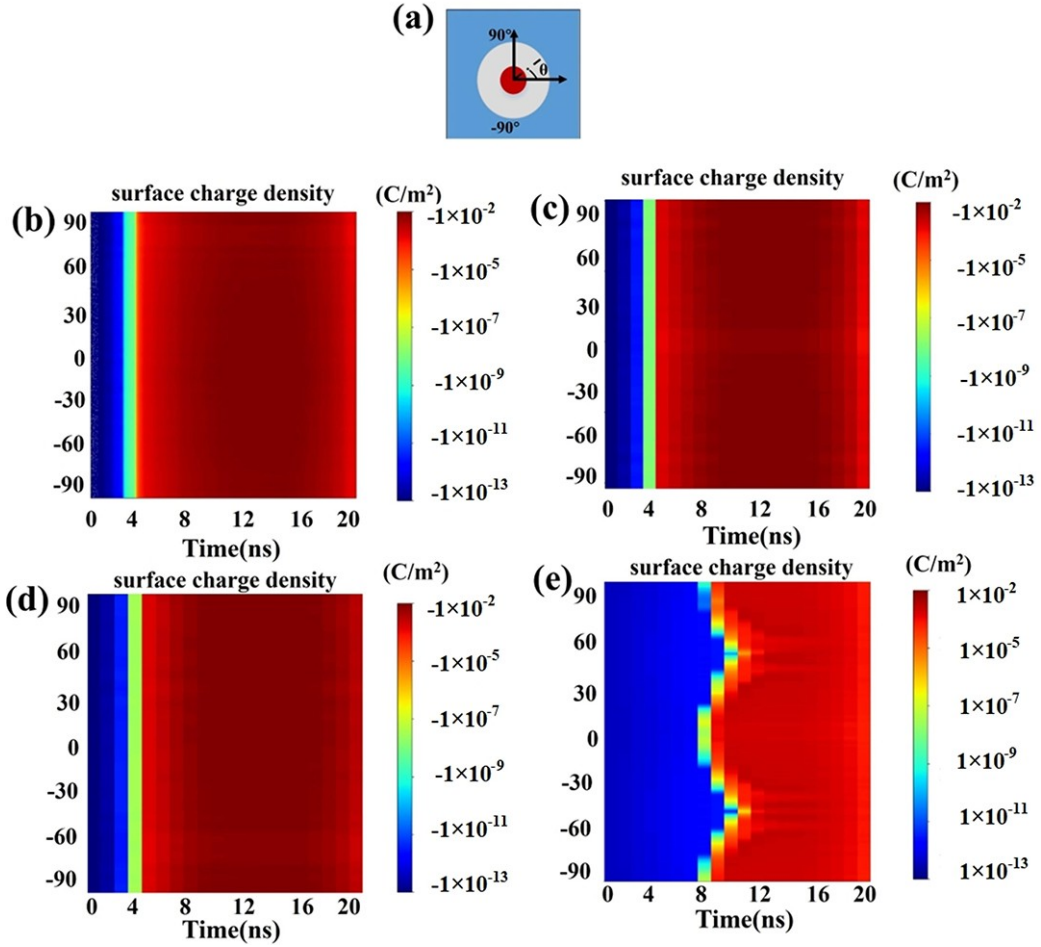

Figure 13. (a) Polar coordinates of the inner dielectric, (b) and (c) spatiotemporal distribution of surface charges on the inner dielectric for positive streamers with CO_2/H_2 volume ratios of 4:1, 2:1 and 1:1, and (e) distribution for negative streamers with a CO_2/H_2 volume ratio of 2:1.

electric field and particle density gradient. In addition, compared to positive streamer discharge, the surface charge density during negative streamer discharge exhibits a non-uniform distribution, as shown in figure 13(e). This may be related to the non-uniform distribution of electrons on the inner dielectric surface, as depicted in figure 2(d4).

4. Conclusion

This study establishes a 2D fluid model for atmospheric-pressure coaxial double-layer DBD plasma CO_2 hydrogenation based on PASSKEy, focusing on the discharge characteristics of streamer discharge under CO_2/H_2 volume ratio, positive and negative nanosecond pulse excitations, and the presence or absence of dielectric sphere filling. Numerical simulation results indicate that, in the positive streamer discharge, as the hydrogen content increases, the discharge channel becomes more confined, with the local electric field strength at the streamer head increasing, leading to faster propagation and a higher surface charge density on the inner dielectric layer. In contrast, the negative streamer discharge shows a more diffuse and uniform discharge channel that nearly fills the entire discharge gap. The model replaces photoionization with seed electron pre-ionization, leading to a higher energy deposited in negative streamer compared to positive streamer, which is responsible for the faster propagation speed, higher space-averaged densities of methanol, and larger accumulated surface charge density in negative streamer discharge. Due to the filling of dielectric spheres, although the methanol produced by PBDBD is confined to inner dielectric spheres, its density is much higher than that of the DBD without dielectric sphere filling, which may be attributed to local electric field enhancement induced by the polarization of the dielectric spheres.

Acknowledgments

This work was in part financially supported by National Natural Science Foundation of China (Nos. 12475261, 12065019 and 12405296). The authors thank Dr Chenhua Ren and Dr Yifei Zhu for their helpful discussions.

Data Availability

The data that support the findings of this study are available from the corresponding author upon reasonable request.

References

[1] Chen S *et al* 2023 *CATENA* **225** 107015
[2] Razali N A M *et al* 2012 *Renew. Sustain. Energy Rev.* **16** 4951
[3] Snoeckx R and Bogaerts A 2017 *Chem. Soc. Rev.* **46** 5805
[4] Sengupta T and Khanna S N 2022 *J. Phys. Chem. A* **126** 5702
[5] Zeng Y X and Tu X 2015 *IEEE Trans. Plasma Sci.* **44** 405
[6] Verheyen C *et al* 2020 *Plasma Sources Sci. Technol.* **29** 095009
[7] Aerts R, Martens T and Bogaerts A 2012 *J. Phys. Chem. C* **116** 23257
[8] Snoeckx R *et al* 2015 *RSC Adv.* **5** 29799
[9] Ozkan A *et al* 2016 *Plasma Sources Sci. Technol.* **25** 025013
[10] Nunnally T *et al* 2011 *J. Phys. D: Appl. Phys.* **44** 274009
[11] Wang W Z *et al* 2016 *Plasma Sources Sci. Technol.* **25** 065012
[12] Sun S R *et al* 2017 *J. CO_2 Util.* **17** 220
[13] Trenchev G *et al* 2019 *Chem. Eng. J.* **362** 830
[14] Klarenaar B L M *et al* 2019 *Plasma Sources Sci. Technol.* **28** 035011
[15] Naidis G V and Babaeva N Y 2021 *Plasma Sources Sci. Technol.* **30** 105016
[16] Moss M S *et al* 2017 *Plasma Sources Sci. Technol.* **26** 035009
[17] Mahdikia H *et al* 2023 *Plasma Chem. Plasma Process.* **43** 2035
[18] Pornmai K *et al* 2019 *Ind. Eng. Chem. Res.* **58** 6203
[19] Wu Y Q Study on the conversion of carbon dioxide by microwave plasma technology in: *Proceedings of 2015 2nd International Conference on Machinery, Materials Engineering, Chemical Engineering and Biotechnology* Chongqing: Atlantis Press 2015: 570–573
[20] Li R Y *et al* 2024 *Spectrosc. Spectral Anal.* **44** 688 (in Chinese)
[21] Douat C *et al* 2023 *Plasma Sources Sci. Technol.* **32** 055001
[22] Barkhordari A *et al* 2021 *Pramana-J Phys.* **95** 1
[23] Wang B W, Wang X X and Zhang B 2021 *Front. Chem. Sci. Eng.* **15** 687
[24] Navascués P *et al* 2022 *Chem. Eng. J.* **430** 133066
[25] Wang Y L *et al* 2024 *Chem* **10** 2590
[26] de la Fuente J F *et al* 2016 *Int. J. Hydrogen Energy* **41** 21067
[27] Zhang X M *et al* 2024 *Plasma Process. Polym.* **21** 2300215
[28] Zeng Y X *et al* 2023 *Ind. Eng. Chem. Res.* **62** 19629
[29] Cui Z L *et al* 2022 *ACS Catal.* **12** 1326
[30] Sun Y H *et al* 2022 *JACS Au* **2** 1800
[31] Wang L *et al* 2018 *ACS Catal.* **8** 90
[32] Zhu Y F *et al* 2021 *Plasma Sources Sci. Technol.* **30** 075025
[33] Li X R *et al* 2024 *Plasma Sources Sci. Technol.* **33** 095009
[34] Kolev S *et al* 2020 *J. Phys.: Conf. Ser.* **1492** 012007
[35] Wang X C *et al* 2022 *Vacuum* **203** 111200
[36] Kourtzanidis K 2023 *Plasma Sources Sci. Technol.* **32** 105016
[37] Cheng H *et al* 2020 *Catal. Today* **351** 103
[38] Du J *et al* 2022 *Plasma Process Polym.* **19** 2100111
[39] De Bie C, van Dijk J and Bogaerts A 2016 *J. Phys. Chem. C* **10** 1021
[40] Liu M *et al* 2019 *Catalysts* **9** 275
[41] Ponduri S *et al* 2016 *J. Appl. Phys.* **119** 093301
[42] Chen Y L *et al* 2022 *Jpn. J. Appl. Phys.* **61** 086001
[43] Liao Y K *et al* 2020 *J. Appl. Phys.* **128** 233303
[44] Brandenburg R 2017 *Plasma Sources Sci. Technol.* **26** 053001
[45] Zhu Y F *et al* 2021 PASSKEy code [software]. Available from http://www.plasma-tech.net/parser/passkey/ (Science and Technology of Plasma Dynamics Laboratory, Xi'an, China and Laboratoire de Physique des Plasmas, Paris, France, 2021).
[46] Bagheri B, Teunissen J and Ebert U 2020 *Plasma Sources Sci. Technol.* **29** 125021
[47] Ren C H *et al* 2023 *Plasma Chem. Plasma Process.* **43** 1613
[48] Zhu Y F and Starikovskaia S 2018 *Plasma Sources Sci. Technol.* **27** 124007
[49] Peng B F *et al* 2024 *Plasma Sources Sci. Technol.* **33** 045018
[50] Hagelaar G J M and Pitchford L C 2005 *Plasma Sources Sci. Technol.* **14** 722

[51] See www.lxcat.net for "Itikawa database"
[52] See www.lxcat.net for "Morgan database"
[53] Itikawa Y 2002 *J. Phys. Chem. Ref. Data* **31** 749
[54] Kozák T and Bogaerts A 2014 *Plasma Sources Sci. Technol.* **23** 045004
[55] Qian M Y *et al* 2018 *AIP Adv.* **8** 125224
[56] De Bie C, van Dijk J and Bogaerts A 2015 *J. Phys. Chem. C* **119** 22331
[57] Zhu Y F *et al* 2017 *Plasma Sources Sci. Technol.* **26** 125004
[58] Liu J B *et al* 2019 *J. Phys. D: Appl. Phys.* **52** 284001
[59] Wang W Z, Butterworth T and Bogaerts A 2021 *J. Phys. D: Appl. Phys.* **54** 214004
[60] Seeger M *et al* 2017 *J. Phys. D: Appl. Phys.* **50** 015207
[61] Zhang Q Z *et al* 2021 *Plasma Process. Polym.* **18** 2000234